# LANGMUIR

pubs.acs.org/Langmuir Article

# Influence of Substitutional Groups on the Ordering and Crystallization of Amphiphilic Silsesquioxanes at the Air-Water Interface

Utsav, Wei Bu, Binhua Lin, and Rupak Banerjee\*



Cite This: Langmuir 2021, 37, 6232-6242



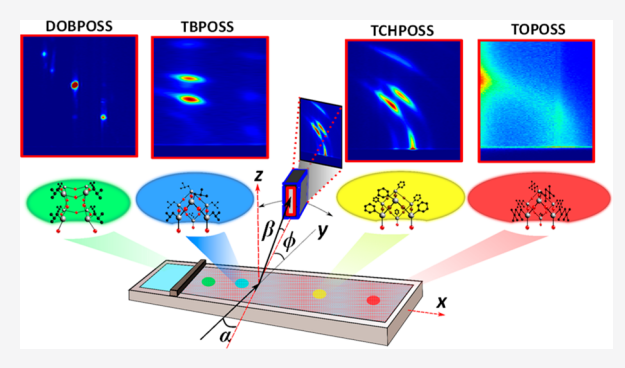
**ACCESS** I

III Metrics & More



S Supporting Information

ABSTRACT: We report on the surface ordering and crystallization sequences in differently organic-substituted amphiphilic polyhedral silsesquioxane (POSS) variants induced by regulated compression at the air—water interface. Such molecular systems floating at the interface serve as a model system to study dynamic crystallization mediated by weak interactions. In situ grazing incidence X-ray scattering (GIXS) measurements, performed at a synchrotron X-ray source using a liquid surface diffractometer and corroborated with Brewster angle microscopy, revealed transformations for the different POSS variants (viz. trisilanol isobutyl POSS (TBPOSS), trisilanol cyclohexyl POSS (TCHPOSS), disilanol octaisobutly POSS (DOBPOSS), and trisilanol isooctyl POSS (TOPOSS)) from a weakly correlated monolayer



structure to appreciably different structural and crystalline phases in various packing schemes. GIXS measurements revealed a stable nature of the crystallization of DOBPOSS, varying degrees of metastable crystallization for TCHPOSS and TBPOSS, and complete absence of crystalline phase in TOPOSS molecules. Incidentally, for all POSS variants showing crystalline phases, the motifs always assembled in a triclinic lattice with PI symmetry. For the metastable crystals, preferential surface ordering of the crystallites promotes selective crystalline planes to exhibit preferred tilt angles with respect to the interface. The structural transformations of the differently substituted POSS molecules and their variations therein are attributed to the changing balance of the hydrophobic vs hydrophilic interaction in the layers, which is determined by the anisotropic shape and distribution of substitutional groups over the nanosized core cage of the monomer, steric interaction between nearest dimeric neighbors, as well as the in-plane and out-of-plane assembly of the overlayers.

# **■ INTRODUCTION**

Surfaces and interfaces formed by molecular assemblies provide a platform to study interactions at a molecular level, where weak, noncovalent, and other forces of different nature and strength play a significant role. The boundaries between solid and gas are static in terms of molecular density fluctuations and serve as an abrupt boundary. In contrast, an interface containing one liquid phase provides a unique boundary with exciting properties. Molecules with amphiphilicity, i.e., polar head and nonpolar tail configuration, orient themselves at the air-water interface with a molecular layer thickness. The monolayer assembly in a confined interfacial area of dynamical nature shows various phases of crystallinity and assemblies depending on the available interfacial area and properties of the interface. Crystallization at the air-water interface is demonstrated by amphiphilic molecules of varying degrees of complexities, ranging from long-chain fatty acids to complex organic-inorganic hybrid molecules.<sup>2</sup> The formation of crystalline structures at the air-water interface, observed through grazing incidence X-ray scattering (GIXS), either in situ or post-transfer to a substrate, has been a field of interest due to the unique interplay of underlying forces driving the assembly at lower dimensions.

Polyhedral oligomeric silsesquioxane (POSS) cage structures (also commonly known as siloxane) have a unique organic—inorganic hybrid nature, where the rigid inorganic core contains silicon (Si) and oxygen (O) atoms, and the organic contribution emanates from the substituents at the edges of the tetravalent Si atoms. POSS frameworks are synthesized either in partially or completely condensed forms. This versatility in the functionalization allows POSS molecules to be synthesized in different molecular structures, having a plethora of physicochemical properties and applications. The nature, position, and the number of substituents over the POSS framework, dictate the fine-tuning of amphiphilicity of a

Received: February 11, 2021 Revised: May 4, 2021 Published: May 10, 2021





functionalized POSS monomer.<sup>6</sup> Self-assembly of selectively substituted open-cage POSS and the consequent effect on the properties of Langmuir monolayers has been studied by Dutkiewicz et al. Self-association and wetting properties of Langmuir-films, utilizing POSS substituted with ethylene glycol and dipalmitoylphosphatidylcholine, show various structural configurations under the influence of surface modifications of the POSS core.<sup>8,9</sup> The customized polarity and reactivity of POSS monomers, along with nontoxicity, thermal stability, and biocompatibility, facilitate their implementation in a wide range of applications. 10 The tailored physicochemical properties of the POSS molecules allow them to be used in grafting, blending, and copolymerizing to alter the mechanical strength, thermal stability, glass transition temperature, or crystallization process. 11,12 An exhaustive study of self-assembly of hybrid-polymers utilizing POSS core framework can be found in the review article by Zhang et al. 13 Artificially prepared biocompatible advanced materials employ the POSS framework due to their nanosize and robust chemical framework to synthesize bioengineered tissue materials, biocomposites, luminophores, and optical sensors. 14,15 POSS nanocages have been utilized to fabricate photosensitive molecular switches, which demonstrated a unique reversible transformation between cubic lattice and helical superstructures. 16 Along with these applications, POSS molecules have been the base structure for many patents and technological advancements in coating applications ranging from the water-resistive paint industry to space survival coating.<sup>17</sup> Unique assemblies formed by controlling positional interactions of a giant tetrahedral molecule containing selectively functionalized POSS cages attached to a tetrahedral core have been reported to form supramolecular structures.<sup>13</sup> The POSS framework's versatility to be incorporated in applications pertaining to advanced plastics, energy conversion and storage devices, space survivable coating, and biomedical applications<sup>19</sup> comes from the fact that the POSS molecules work as models for active surface sites suitable for functionalization. These hybrid materials are applicable for fire repellent, nanofillers for reinforced plastics and rubber, dental nanocomposites and drug delivery material, and labbased tissue engineering exploiting the propensity of POSS materials to self-assemble in low dimensions.2

POSS derivatives of different amphiphilicity self-assemble to form hierarchical structures, where the morphological properties are primarily dependent on noncovalent interactions. Understanding the interactions dictating the assembly in POSS layers is of utmost importance for tuning the effective physicochemical properties of the transferred layer. The observed crystallinity within the floating layers at the airwater interface emanates from the organization of the dimers.<sup>21</sup> The dimerization in the heptameric  $(T_7)$  and octameric  $(T_8)$ POSS frameworks originates from the weak H-H bonding between the Silanol bonds. The spectroscopic studies investigating the dimerization mechanism of the heptameric and octameric POSS monomers show existence of dynamic equilibrium between their monomeric and dimeric forms.<sup>22</sup> The self-assembly of different POSS monomers depends on a variety of factors and interactions such as size, structure, polarity, reactivity, and electron density of the substituents, along with the properties of the POSS cage, the position of the substituent with respect to the core, and relative orientation of the substituents with respect to each other.<sup>23–26</sup> POSS cages can be synthesized to have a closed-cage condensed structure

(8 Si-atoms)<sup>27</sup> or an open-cage uncondensed structure (7 Siatoms).<sup>28</sup> Trisilanol cyclohexyl polyhedral oligomeric silsesquioxane (TCHPOSS) monomers and phosphorus-containing polyimide matrix nanocomposite thin films have been explored for their antioxidative properties in high radiative and atomic oxygen environment for upper atmosphere survivability. 29,30 The existence of reversible monolayer to crystalline phase transitions of Trisilanol Isobutyl POSS (TBPOSS) at airwater interface was demonstrated using synchrotron X-ray scattering,<sup>31</sup> and the reversibility was attributed to the existence of metastable crystalline phases. This opened up new avenues of research for reversible phase transitions in synthesized materials with the potential of mimicking reversible crystallization, which has been observed naturally in the tendons of animal tissues<sup>32</sup> and proton pumping mechanism in bacteriorhodopsin.<sup>33</sup> Insight into the details of the structural assembly and path followed by the layers of amphiphilic POSS at the air-water interface, pre-, and posttransition, in various cycles of compression and decompression, could be potentially used for controlled fabrication of ultrathin films with interesting physicochemical properties.<sup>34,35</sup>

Characterizing the structural arrangement of POSS monomers poses a significant challenge due to the weak scattering nature of the organic—inorganic framework, thus necessitating an intense, highly monochromatic, and collimated beam of X-rays available only at the synchrotron facilities. Further, since the balance of the hydrophobic vs hydrophilic interactions is maintained only at the air—water interface (and not when transferred to a solid substrate), the availability of a liquid surface diffractometer (with a Langmuir trough atop) at the synchrotron facility is essential to perform scattering measurements at the air—water interface. Thus, the proper alignment, reproducible measurements, data acquisitions, and analysis are arduous and challenging, particularly when the sample is probed in situ.

In the present work, we employ different variants of substituted POSS molecules (using uncondensed heptameric and octameric open-cage POSS framework) with a varying degree of amphiphilicity (determined by the nature of the substitutional groups, the Silanol bonds and, their relative positions) to explore the interplay of hydrophobic and hydrophilic interactions guiding the ordering, structural transformations and crystallization of the floating POSS layers using in situ GIXS and Brewster angle microscopy measurements. Quantitative analysis reveals details about the nature of the crystallization in the differently substituted POSS variants and the crucial role of amphiphilicity in the assembly of monomeric POSS variants starting from a sparsely populated interface to a stable, unstable, or nonexistent crystalline state. The study thus provides an insight into the dynamic nature of molecular crystallization mediated by weak Van der Waal's interactions and strongly influenced by the organic-substitutions of the amphiphilic molecules at the air-water interface.

#### EXPERIMENTAL SECTION

Differently substituted POSS molecules were purchased from Hybrid Plastics, U.S.A., and used for experiments without further purification. The POSS variants used in the experiments are trisilanolisobutyl polyhedral oligomeric silsesquioxane (TBPOSS) (Figure 1(a)), trisilanol cyclohexyl polyhedral silsesquioxane (TCHPOSS) (Figure 1(b)), trisilanol isooctyl polyhedral oligomeric silsesquioxane (TOPOSS) (Figure 1(c)), and disilanolisobutyl polyhedral silsesquioxane (DOBPOSS), (Figure 1 (d)). The empirical formula corresponding to these compounds is  $C_{28}H_{66}O_{12}Si_7$ ,  $C_{32}H_{74}O_{13}Si_8$ ,  $C_{42}H_{80}O_{12}Si_7$ ,

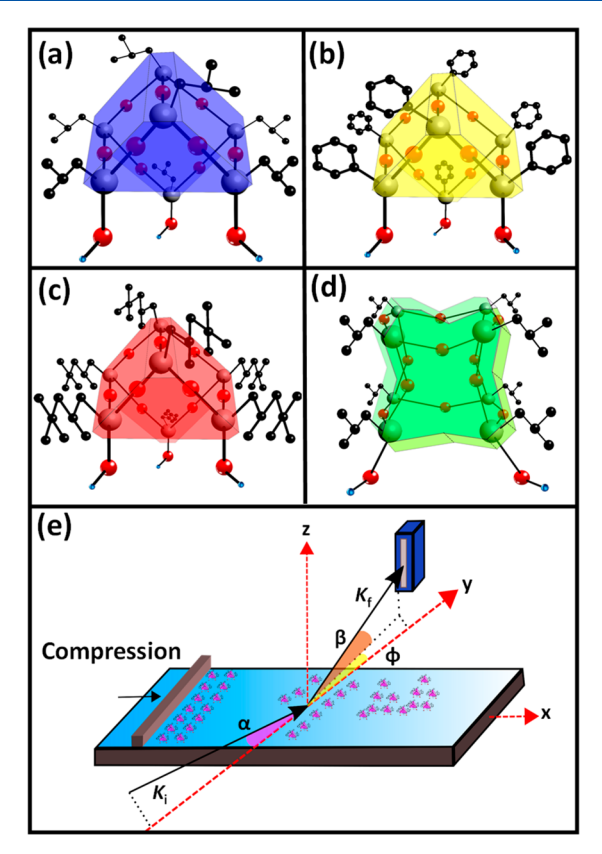


Figure 1. Skeletal representation for the (a) TBPOSS, (b) TCHPOSS, and (c) TOPOSS monomer showing heptameric POSS frame carrying three silanol bonds with isobutyl, cyclohexyl, and isooctyl substitution, respectively. Skeletal rendering of (d) DOBPOSS monomer showing octameric POSS framework with two silanol bonds and isobutyl groups at the surface sites. (e) Schematic representation of liquid-surface diffraction geometry for GIXS measurements at the air—water interface over a Langmuir trough.

and  $C_{56}H_{122}O_{12}Si_7$  for TBPOSS, DOBPOSS, TCHPOSS, and TOPOSS, respectively. Colloidal solutions of a given concentration (0.3 mg/mL) of each POSS variant were prepared by dispersing the monomers in Chloroform (Sigma-Aldrich) and then ultrasonicated at 25 °C for 30 min. Primary investigations of existing phases and stability of the films were tested by carefully spreading 25  $\mu$ L of freshly prepared aliquot at the air—water interface of a double-barrier Langmuir trough (APEX Instruments, India). The interface was left undisturbed for 1 h, allowing solvent evaporation and then compressed at a steady rate of 1 mm/min to record surface pressure vs area isotherm.

X-ray scattering measurements were performed at ChemMatCARS, Sector 15-ID-C, Advanced Photon Source, Argonne National Laboratory (U.S.A.) using 10 keV ( $\lambda$  = 1.24 Å) X-ray beam, aligned at a fixed incidence angle of  $\alpha = 0.1^{\circ}$ . The incidence angle is chosen to be smaller than the critical angle of the water subphase (which is 0.123° at this wavelength), thus probing only the floating POSS layers. The scattering geometry during the measurement of in-plane and out-of-plane scattering with a one-dimensional (1-D) Pilatus detector (Dectris) of pixel size  $172 \times 172 \ \mu\text{m}^2$  is shown in Figure 1(e). The 2-D scattered intensity profiles were obtained by scanning the 1-D detector along the in-plane angle  $(\varphi)$  and stitching them together. The 2-D scattering profile thus demonstrates the variation in the scattered intensity as a function of momentum transfer vector (Q) resolved in the in-plane  $(Q_{xy})$  and out-of-plane  $(Q_z)$  directions. The  $Q_{xy}$  and  $Q_z$  values are related to the in-plane  $(\varphi)$  and out-of-plane  $(\beta)$ angular movement of the detector and provide information about the structural ordering of the sample along the in-plane and the out-ofplane directions, respectively. The beam is defined by the incident

slits before the interface (0.1  $\times$  2 mm²), and the instrumental resolution is 0.01 Å $^{-1}$  in the  $Q_{sy}$  direction. The colloidal solutions were spread at a custom-built single barrier trough filled with deionized water (control system from NIMA, U.K.) of a usable area of 215 cm². The chamber was purged with Helium to reduce the Oxygen content to 1% of the atmospheric levels to ensure minimum background scattering. The subphase temperature was maintained at 10 °C to stabilize the interface and minimize capillary wave fluctuations.

The barrier was compressed slowly (at a speed of 1.1 mm/min) until the target pressure was achieved. GIXS measurements were performed at specific values of surface pressure during different cycles of compression and decompression. These surface pressures were suitably chosen such that each measurement point represents a particular structural phase as indicated by the surface pressure vs area per molecule isotherm. Data acquisition rate and beam damage were carefully monitored for optimized and reproducible scattering intensity. Bulk crystallinity of the pristine powdered sample of each POSS variant was characterized using a  $Cu-K_{\alpha}$  ( $\lambda=1.54$  Å) lab source diffractometer (Smartlab 9 KW, Rigaku Corporation, Japan).

Brewster angle microscopy (BAM) measurements on Langmuir monolayers of POSS molecules were performed with KSV NIMA MicroBAM (Biolin Scientific, Finland) setup having a linear resolution of 12  $\mu$ m, attached to a trough of interfacial area 24 300 mm<sup>2</sup> (KSV NIMA Langmuir-Blodgett Medium Trough-KN 2002, Biolin Scientific, Finland). An area of  $3.6 \times 4 \text{ mm}^2$  was probed with a charge-coupled device camera coupled to a diode LASER of wavelength 659 nm, fixed at an angle of incidence of 53° with respect to the normal at the air-water interface. The interface was symmetrically compressed, and images of the floating monolayer were acquired while monitoring the surface pressure. The assistance of auto gain control mode was utilized to obtain images with higher contrast and desired sensitivity. Images were acquired at those surface pressures at which GIXS measurements were performed so that the scattering features could be mapped with the corresponding morphological features of different POSS layers under compression-decompression cycles.

## ■ RESULTS AND DISCUSSION

The core structure of the POSS molecular framework (i.e., Heptameric and Octameric Si-O framework), as well as the substitution of the core with different hydrophobic and hydrophilic groups, dictate the overall amphiphilicity and the ensuing physiochemical properties of the POSS variant.<sup>36</sup> Monomers of POSS variants with isobutyl and cyclohexyl substitution groups with trisilanol heptameric framework are known to have structural phase transitions of dynamical nature. 31,37 We subsequently choose molecules that are either similar in their exostructure to TBPOSS but have different substitutional groups or have a different exostructure than heptameric POSS retaining the same substitutional group. The schematic representation of the POSS monomers is shown in Figure 1(a-d) for TBPOSS, TCHPOSS, TOPOSS, and DOBPOSS, respectively. The chemical and physical properties of the POSS variants can be referred to the PubChem database, using PubChem ID's of 4381659, 4549737, 3455088, and 5071479 for TBPOSS, TCHPOSS, TOPOSS (similar structure), and DOBPOSS molecular structures, respectively. DOBPOSS molecules possess one less silanol bond but one excess isobutyl substitution, with a more condensed cage structure than TBPOSS. DOBPOSS molecule possesses an octameric framework, with regular-exo-Silanol in contrast to Zexo (opposite corner of the same face) structure.<sup>38</sup> The substitutional group variation over a POSS cage changes the net amphiphilicity of the molecule, thus influencing the ordering mechanism and structural organization at the

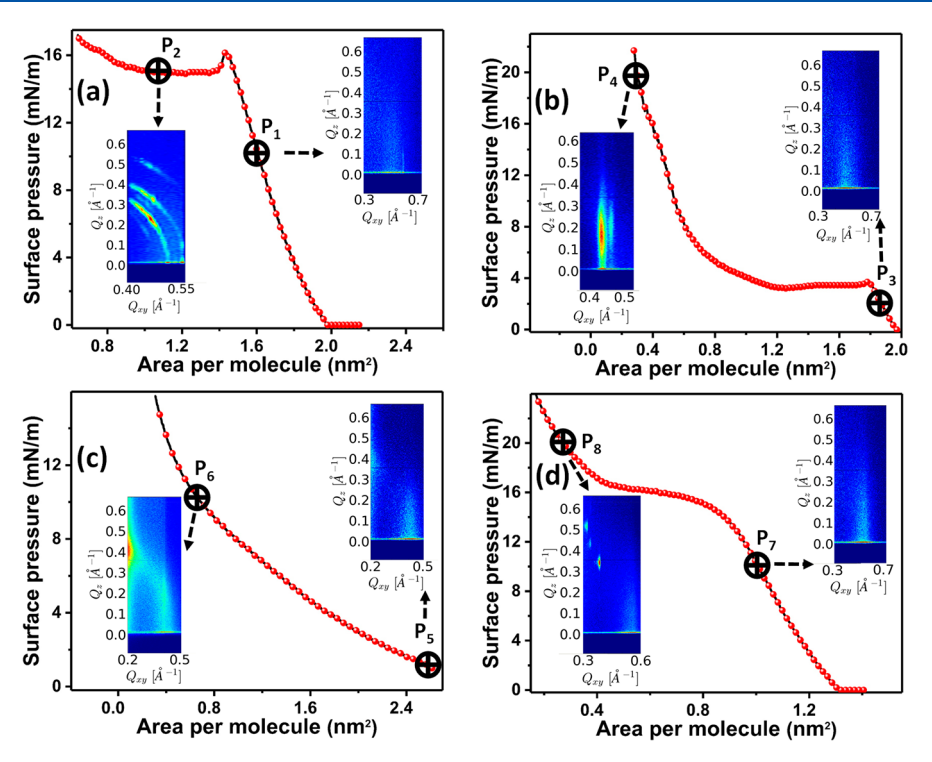


Figure 2. Measured surface pressure versus area per-molecule isotherm during  $1^{\rm st}$  cycle of compression with designated target surface pressure values selected for GIXS measurements for (a) TBPOSS layer, showing correlation peak prior to collapse at  $P_1 = 10$  mN/m and Debye–Scherrer ring formation postcollapse at  $P_2 = 16$  mN/m, (b) TCHPOSS layer, showing correlation peak at surface pressure value  $P_3 = 2.5$  mN/m, prior to collapse, before transitioning to a correlated bilayer structure at surface pressure  $P_4 = 20$  mN/m, exhibiting twin Bragg-rod intensity profile, (c) TOPOSS layers, showing in-plane and out-of-plane correlation peaks at surface pressure ( $P_5 = 1.5$  mN/m) and enhanced correlation peaks that show arching at higher compression  $P_6 = 10$  mN/m, and (d) DOBPOSS layer, showing monolayer correlation peak at  $P_7 = 10$  mN/m and its subsequent transition into a crystalline state postcollapse at pressure  $P_8$  corresponding to 20 mN/m. The measured diffractograms corresponding to the target surface pressure are shown alongside.

interface. Trisilanol POSS variants (viz. TBPOSS, TCHPOSS, and TOPOSS) have a typical cage size of 1-1.2 nm,<sup>39</sup> while DOBPOSS having an octameric framework, has a smaller size of 0.5 nm. 40 The difference in the TCHPOSS and TOPOSS monomers originates from the chain-length of the organicsubstituents and the corresponding exclusion volume of the monomers. The stability of the floating layers at the interface is determined by the balance of hydrophilic interaction between -OH groups with the subphase and the hydrophobic interactions due to the presence of the substitutional groups. Amphiphilic POSS monomers serve as model systems for the investigation of weak-interaction mediated assemblies.<sup>41</sup> The amphiphilic POSS monomers spread at the air-water interface exhibit variation in surface pressure with respect to a change in the interfacial area. The liquid surface diffractometer setup fitted with a sensitive tensiometer facilitates in situ GIXS measurement (schematically shown in Figure 1(e)) at different surface pressure values.

The behavior of the surface pressure (SP) vs area isotherm serves as a primary indicator of the presence of different structural phases and phase transitions. SP vs area per molecule isotherm was recorded for the first compression cycle of all POSS variants and is shown in Figure 2. GIXS measurements were performed at specific surface pressures corresponding to a particular structural phase. These SP values are denoted as "P" with a subscript, and the GIXS patterns acquired at these pressure are indicated by arrows in Figure 2. TBPOSS monolayer collapses at a SP of 15 mN/m (corresponding to the area per molecule 1.5 nm²), as shown

in Figure 2(a). GIXS measurement at a SP of 10 mN/m (denoted as  $P_1$ ) below the collapse pressure demonstrates a diffused scattering peak centered around 0.53 Å $^{-1}$ , corresponding to an in-plane correlation length of 11.85 Å. This is characteristic of a monolayer phase where the position of the in-plane correlation peak determines the in-plane separation between the neighboring molecules. The diffraction profile measured beyond the collapse pressure (denoted as  $P_2$ ) exhibits a diffraction pattern resembling polycrystalline behavior as evident by the Scherrer rings interspersed with intense spots indicative of preferential ordering of some crystal planes.

The GIXS measurement was next performed on the TCHPOSS monolayer at SP of 2.5 mN/m (denoted by P<sub>3</sub> in Figure 2(b)). The GIXS profile reveals a weak correlation between TCHPOSS monomers floating at the air-water interface. The scattered intensity (line-cut) profile obtained by integrating  $Q_z$  values (between 0.0 and 0.5 Å<sup>-1</sup>) estimates the correlation peak to be centered around  $Q_{xy} = 0.46 \text{ Å}^{-1}$  and translates to a real space correlation distance of 13.65 Å (Figure S1(a) in the Supporting Information, SI). Further compression of the TCHPOSS monolayer leads to the collapse of the monolayer (at a SP of 3.5 mN/m), characterized by a sharp dip followed by almost no change in the SP, even after continued compression as observed in Figure 2(b). The structural configuration of amphiphilic layers postcollapse pressure is generally characterized by distortion in the monolayer configuration, and further barrier compression transfers molecules on top of the collapsed monolayer. 43 The

amphiphilicity of the molecule dictates the ease of transfer to the top layer. POSS molecules are known to undergo dimerization postcollapse. The dimerization phenomenon holds two monomers together in a locked position relative to each other by three Silanol bonds, which are slightly tilted outward from their monomeric framework positions. The dimerization process is due to weak OH-OH bonds forming between the hydrophilic groups of the TCHPOSS.44 In contrast, the relative position of the hydrophobic and hydrophilic substitutional groups decides the packing behavior over the monolayer. 45,46 The SP remains constant for a considerable compression (wherein the area/molecule changes from 1.75 nm<sup>2</sup> to about 1.2 nm<sup>2</sup>) beyond the collapse pressure. GIXS measurement at a pressure of 3.45 mN/m postcollapse exhibits a well-defined single Bragg rod at  $Q_{xy} = 0.46 \text{ Å}^{-1}$  and  $Q_z = 0.20 \text{ Å}^{-1}$ , as shown in Figure S1(b) in the SI. The inplane correlation length is estimated by taking line-cuts along  $Q_{xy}$  and turns out to be 13.65 Å, and the out-of-plane correlation length (taking similar line cuts along Q<sub>s</sub>) is found to be 30.2 Å. Analyses of the rod profile obtained postcollapse during first and second cycle for the TCHPOSS layer, using the Scherrer formula revealed an in-plane and an out-of-plane crystallite size of around (366 Å, 30 Å), and (402 Å, 41 Å), respectively. Under extreme compression, TCHPOSS layers show preferred orientations, and an approximate crystallite size for the strongest diffracting peak (100) was obtained to be 606 and 188 Å, in the in-plane and out-of-plane directions, respectively. Crystallite sizes corresponding to the prominent peak seen in the TBPOSS layers at extreme compression were estimated to be 1018 and 399 Å in the in-plane and out-ofplane directions. DOBPOSS layers exhibit diffraction spots, characteristic of a single-crystal like structure, where the crystallite size corresponding to the prominent (112) peak was observed to be around 1638 Å. The diffractogram corresponding to the extreme compression denoted as P4 shows two Bragg rods separated in both  $Q_{xy}$  and  $Q_z$  space. The intensity profile corresponding to this Bragg rod profile is shown in Figure S1(c) in the SI.

The TOPOSS isotherm lacks any distinct structural transition feature, as evident from Figure 2(c). The diffractogram corresponding to SP of 1.5 mN/m (denoted by  $P_5$ ) exhibits a weak correlation peak in both in-plane and out-ofplane directions, which subsequently intensifies and demonstrates arching of correlation peak indicating buckling in the layers, as the surface pressure is increased to  $P_6$ . The weak correlation peak positions observed at  $Q_{xy} = 0.40 \text{ Å}^{-1}$  and  $Q_z = 0.40 \text{ Å}^{-1}$ 0.35 Å<sup>-1</sup>, and the corresponding length scales for in-plane and out-of-plane ordering were calculated to be 15.56 and 17.56 Å, respectively. The octameric DOBPOSS isotherm shows a takeoff area of 1.3 nm<sup>2</sup> (in accordance with its smaller size compared to heptameric POSS variants) and collapses at a SP of 15 mN/m corresponding to a molecular area of 0.8 nm<sup>2</sup>. The dynamical phase immediately after the collapse is characteristic of all the POSS variants (apart from the TOPOSS). For DOBPOSS, this phase extends from an area/ molecule value of 0.8 nm<sup>2</sup> to 0.4 nm<sup>2</sup>. Subsequent compression beyond the 0.4 nm<sup>2</sup> molecular area shows an increase in the SP value with a slope identical to that before the collapse as seen in Figure 2(d). The GIXS measurement at SP prior to collapse, denoted as  $P_7$ , shows a weak correlation peak at  $Q_{xy} = 0.56 \, \text{Å}^{-1}$ corresponding to a monolayer configuration with an interparticle length scale of 11.21 Å. The diffractogram obtained postcollapse at a SP of 20 mN/m (denoted by  $P_8$ )

shows a few distinct diffraction spots similar to a single crystal diffraction pattern along with an interparticle correlation peak (characteristic of a monolayer) in the background.

Relaxing the compressed layers of POSS variants floating at the air—water interface was achieved by regulated withdrawal of the barrier. Multiple cycles of compression and decompression highlight the difference between the isotherms of trisilanol POSS variants (TBPOSS, TCHPOSS, and TOPOSS) and the disilanol POSS (DOBPOSS) variant. The surface pressure for trisilanol POSS variants falls sharply; whereas the disilanol POSS isotherm retraces the same path during both the first and second compressions. GIXS measurements were performed on the decompressed layers, but for most of the POSS variants, the scattering profile demonstrates a weak interparticle correlation peak (refer to Figure S2 in the SI).

The relaxed interface was again recompressed at a rate of 1.1 mm/min for a second cycle, and the respective isotherms are shown in Figure 3(a-d). POSS molecules are well-known for their stability at the air-water interface; however, the area per molecule for surface pressure onset during the second compression cycle was observed to decrease compared to the first compression cycle. The collapse phase, however, reoccurs at the same surface pressure during both compression cycles for TBPOSS, TCHPOSS, and DOBPOSS monomers (Figure 3(a), (b), and (d), respectively), allowing an estimation of the fraction of the spread area present as a monomer during the second compression cycle. In other words, if there is no loss of molecules, then the extent of reversibility of phases due to the relaxation of lateral stress could be quantified. We define the reversibility factor as the ratio of the area per molecule at the onset of surface pressure for consecutive isotherm cycles. For the perfect reversibility of a monolayer to either a dimeric or a crystalline phase (and vice versa), the value of the reversibility factor should be unity, as is almost the case for TBPOSS. TCHPOSS layers do exhibit the repeatable nature of isotherm during different compression cycles, but the reversibility factor is only around 0.46. This shows that there must exist overlayers (on top of the monomers) that do not reverse entirely even when the surface pressure is fully withdrawn, thus explaining the reduced area per molecule (hysteresis in the isotherm seen in Figure 3(b)) during the second collapse. The TOPOSS layer in the second cycle retraces its original surface pressure isotherm (refer to Figure 3(c)). Still, since there was no structural transition to a crystalline phase within the observed SP regime, the reversibility in structural phases cannot be defined in this case. The DOBPOSS layers exhibit a higher reversibility factor of 0.85 estimated from the isotherm shown in Figure 3(d).

GIXS measurements of the POSS variants at SPs beyond the collapse during the second cycle (denoted as  $P_9$ ,  $P_{10}$ ,  $P_{11}$ , and  $P_{12}$  in the isotherms shown in Figure 3(a–d), respectively), exhibit significant differences in their diffraction profiles owing mostly to changes in their substituents. GIXS measurements at  $P_9$  for TBPOSS layers (Figure 3(e)) demonstrates characteristic polycrystalline Debye–Scherrer ring formation with intense diffraction spots and has been previously observed. The intensity profile was fitted, and lattice spacings ( $d_{\rm hkl}$ ) were estimated. Lattice parameters, symmetry, and cell volume were estimated and corroborate previously reported values. The presence of intense spots on the Scherer rings indicate some preferred orientations of the crystalline planes, which are otherwise polycrystalline. The tilt angles of the diffracting planes (with respect to the interface) are estimated using

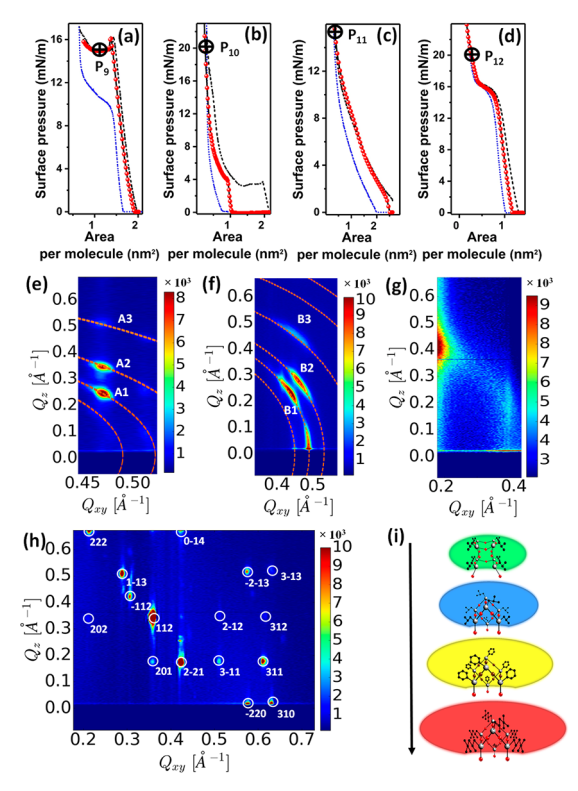


Figure 3. Surface pressure versus area per-molecule isotherm for the second compression showing target surface pressure value of (a)  $P_9$  = 16 mN/m of TBPOSS, (b)  $P_{10} = 20$  mN/m of TCHPOSS, (c)  $P_{11} =$ 13.5 mN/m of TOPOSS and, (d)  $P_{12}$  = 20 mN/m of DOBPOSS layers. (e) GIXS pattern at P9 showing diffraction spots (exhibiting preferred tilt angles of A1, A2, A3) over Scherrer rings fitted for dhkl values (dashed red line) using TBPOSS lattice parameters. (f) GIXS pattern at P<sub>10</sub> shows similar Scherrer rings (with some preferred orientation B1, B2, and B3 of diffracting planes) also fitted with arcs representing  $d_{hkl}$  values corresponding to lattice parameters of TCHPOSS crystal at the interface. The spots, however, are more spread out along the Scherrer ring than those observed for TBPOSS. (g) GIXS measurement at  $P_{11}$  for the TOPOSS layer shows scattering features (interparticle correlation peak arching toward Qz value) similar to buckled phases of a monolayer. (h) GIXS diffraction profile of DOBPOSS layer showing diffraction spots along with the indexed peak positions corresponding to single-crystal phase at a surface pressure of  $P_{12} = 20 \text{ mN/m}$ . (i) Model rendering of POSS variants in an increasing order of exclusion volume (DOBPOSS < TBPOSS < TCHPOSS < TOPOSS) due to hydrophobic substituents.

 $\theta = \tan^{-1} \frac{Q_z}{Q_{xy}}$  and schematically shown in Figure S3(a-c). For the TCHPOSS layers, the GIXS measurements at high

compression  $(P_{10})$  during the second cycle exhibit a diffraction pattern (Figure 3(f)) somewhat similar to the one observed for TBPOSS. The  $d_{hkl}$  values were calculated by fitting the GIXS profile assuming a P1 triclinic structure. The corresponding lattice parameters are, a = 15.319 Å, b = 12.861 Å, c = 13.289Å,  $\alpha = 99.57^{\circ}$ ,  $\beta = 99.41^{\circ}$ , and  $\Upsilon = 110.59^{\circ}$ , with a crystal volume of around 2346  $Å^3$ . The observed and calculated  $d_{hkl}$ values along with the corresponding Miller indices are shown in Table S1 in the SI and are in good agreement with each other, although some peaks are missing in the observed diffractogram. The absence of peaks from the observed diffractogram can be attributed to the fact that the molecular crystal is quite large and held together by weak Van der Waal's forces at the air-water interface. Additionally, the scattering from the floating layers is quite low, and the crystallization process is itself dynamic in nature, induced by regulated lateral pressure on the interface. Each of these  $d_{hkl}$  values corresponding to specific scattering planes exhibits preferred tilt angles with respect to the water surface. The preferred tilt angles of the different scattering planes are schematically shown in Figure S4 for the spots marked as B1, B2, and B3. These preferred tilt angles were estimated to be  $28.8^{\circ} \pm 5.9^{\circ}$ for the (001),  $30^{\circ} \pm 4.6^{\circ}$  for the (010) plane, and  $44.8^{\circ} \pm 4.3^{\circ}$ for the (0-11) plane, respectively. GIXS measurement of TOPOSS layers at SP  $P_{11}$  during the second compression shows a net appreciation in the in-plane and out-of-plane scattered intensity, without any change in the peak positions, as seen in Figure 3(g). However, the change in the intensity increases more in the out-of-plane direction compared to the in-plane direction. This behavior of TOPOSS layers can be attributed to the out-of-plane stacking of a highly viscous fluidlike pristine state of TOPOSS. The arching of the correlation peak also indicates a buckled layer at the interface.

GIXS measurement of DOBPOSS layers at SP of 20 mN/m ( $P_{12}$  in Figure 3 (d)) during second compression results in intense diffraction spots characteristic of single crystals, as shown in Figure 3(h). The integrated line intensity profile along the in-plane ( $Q_{xy}$ ) and the out-of-plane ( $Q_z$ ) direction is shown in Figure SS(a,b), respectively. The diffracted intensity profile was analyzed and solved for the underlying crystal structure. The resultant crystal structure has triclinic PI symmetry (quite characteristic for POSS crystals), with lattice parameters of a = 35.12 Å, b = 35.90 Å, c = 32.15 Å,  $\alpha = 102.55^{\circ}$ ,  $\beta = 78.50^{\circ}$ , and  $\Upsilon = 102.50^{\circ}$ , and the corresponding volume of 38 134 ų, which is an order larger than the reported powder crystal structure. It must be noted, though, that the identification and indexing of all the peaks present in the diffraction pattern are severely limited by the inhomogeneity in

Table 1. Observed Values of Correlation Peaks Corresponding to the Monolayer Phase and Calculated Lattice Parameters, Unit Cell Volume, And Nature of Crystal Formed Post-Collapse during the 2<sup>nd</sup> Compression Cycle of DOBPOSS, TBPOSS, TCHPOSS, and TOPOSS Layers

POSS variant (in order of least to most exclusion volume)	correlation peak position $(Q_{xy}(\mathring{A}^{-1}))$	nature of crystal	calculated lattice parameters $(a, b, c, \alpha, \beta, \gamma)$	unit cell volume (ų)
DOBPOSS	0.56	single crystal	35.12 Å, 35.90 Å, 32.15 Å, 02.55°, 78.50°, 102.50°	38134
TBPOSS	0.53	weakly polycrystalline with strong preferential orientation	<sup>a</sup> 13.82 Å,15.48 Å, 14.01 Å, 88.57°, 110.41°,109.51°	<sup>a</sup> 2635
TCHPOSS	0.46	strongly polycrystalline with weak preferential orientation	15.32 Å, 12.86 Å, 13.29 Å, 99.57°, 99.41°, 110.59°	2346
TOPOSS	0.40	no crystal	NA	NA

<sup>&</sup>lt;sup>a</sup>Denotes that the lattice parameter values were taken from Reference.<sup>31</sup>

the floating films and the low number of observed diffraction spots. Table S2 in the SI lists all the observed and calculated  $d_{\rm hkl}$  values along with corresponding Miller indices for the refined crystal structure.

The monolayer formation at the air—water interface acquires a close-packed assembly, held at the interface by the weak H—H bonding between the silanol bonds and the subphase. The intermolecular separation in the monolayer depends on the exclusion volume of the POSS monomer. The exclusion volume at the air—water interface is dictated by the hydrophobic substituents and POSS framework size. This behavior is evident from the  $Q_{xy}$  values of the correlation peak observed at SP values prior to collapse for different POSS layers. Thus, TOPOSS has the largest exclusion volume and DOBPOSS the least, in the sequence DOBPOSS < TBPOSS < TCHPOSS < TOPOSS, as depicted schematically in Figure 3(i). Table 1 lists the correlation peak positions, nature of crystal formed during the second compression cycle, and the corresponding lattice parameters for different POSS variants.

Brewster's angle microscopy (BAM) measurement on POSS layers shows various stages of aggregation at the air—water interface. The aggregation of POSS monomers postcollapse results in a stark intensity contrast between the subphase and floating aggregates. This intensity contrast difference between different domains within the visualized area originates from the difference in the thickness of the different floating layers. Figure 4 shows BAM images for the different POSS variants

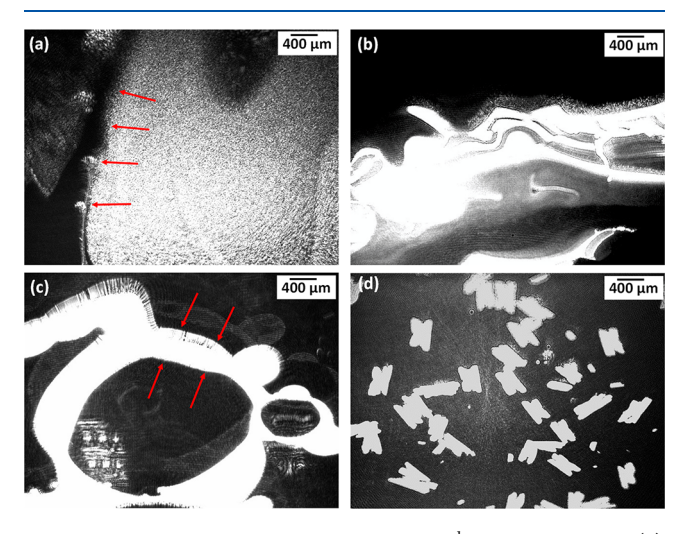


**Figure 4.** BAM images acquired during 2<sup>nd</sup> compression of (a) TBPOSS layer postcollapse showing a sizable interfacial area covered with crystallized TBPOSS dimers in contrast to the subphase, separated by a phase boundary (indicated by arrows), (b) large crystallites of TCHPOSS dimers with sharp edges and low contrast bilayers, formed at high surface pressures, (c) oil-like buckled floating multilayer of TOPOSS (bounded by the arrows) with a sharp contrast with respect to the subphase, and (d) freely floating stable crystallites of DOBPOSS dimers, formed at high compression.

postcollapse in the second compression cycle. BAM image of the TBPOSS layer in Figure 4(a) shows the phase boundary (denoted by arrows) between the subphase and the crystalline layer, evident by the difference in contrast along with a low contrast monolayer phase visible around the corner. The BAM images for floating TCHPOSS layers (Figure 4(b)) show stark intensity contrast between the crystallites and the underlying layers. Crystal facets are also visible in some cases, and overall

the long crystallites seem to be aggregated together in the floating mass of crystalline domains. The BAM images capturing the intermediate stages of the TCHPOSS layer showing structural evolutions during the first compression cycle are shown in Figure S6 in the SI. TOPOSS layers at the interface exhibit oil-like behavior and the corresponding BAM image is shown in Figure 4(c). The phase boundary between the TOPOSS layers and the subphase is clearly visible and is marked by arrows. Evidence of wrinkled or buckled layers with oil-like demixing behavior with the subphase is seen. DOBPOSS layers exhibit stable crystallization, and crystallites floating freely at the interface can be seen in Figure 4(d). X-ray reflectivity measurements were performed over the compressed floating layers of POSS variants, as shown in Figure S7 in the SI. The lack of electron density contrast between the subphase and the POSS layers prohibits any modulation in the reflectivity profile that can be analyzed to extract the out-ofplane ordering and layering of the POSS layers.

Modeling the structural transitions of the different POSS variants at the air-water interface requires a detailed understanding of the stacking mechanism of POSS monomers under the influence of competing weak interaction forces. The assembly at the air-water interface is modeled based on the observed GIXS profile and BAM imaging of the interface during the second cycle and is depicted schematically in Figure 5 for each POSS variant, using the simplified volume exclusion model. Figure 5(a) shows the ordering within the TBPOSS layers, where TBPOSS monomers populate the interface and stay intact due to the hydrogen bonding between TBPOSS monomers and the subphase. The dimerization takes place in the immediate layers above the monolayer, and these dimers arrange themselves in a strongly scattering polycrystalline form. TCHPOSS layers, however, assemble themselves to a polycrystalline state mediated via a correlated bilayer structure, as shown in Figure 5(b). The intermediate stages of the assembly within the bilayers are explained in the SI and shown in Figure S8 in the SI. A model depicting the TOPOSS layers' arrangement at the interface under lateral compression (considering that substituted heptameric POSS molecules inherently exhibit dimerization) is shown in Figure 5(c). The GIXS measurement corresponds to a compressible multilayer lacking any crystalline structure formations. The interface supports the TOPOSS monolayer, over which dimers of TOPOSS form multiple compressible layers, so overall, the layer has a buckled structure. The arcing of the interparticle correlation peak toward Qz values as observed in the GIXS profile (Figure 3(g)) is a characteristic sign of buckling in the TOPOSS multilayer. 49–51 The estimation of this buckling length is restricted by the indistinguishable layering scheme and the presence of the unknown number of the multilayers. DOBPOSS layers exhibit an immediate transition to a single crystal-like phase during the collapse, which is modeled as the repetition of identical units of triclinic crystal structures of DOBPOSS dimers, as shown in Figure 5(d). The dimers of the POSS variant serve as the motifs of the crystal structure.

The bulk form of the different POSS powder sample variants was examined using lab source X-rays and showed prominent peaks at lower diffraction angles but broad peaks at larger diffraction angles, as shown in Figure S9 in the SI. Figure S9(a-d) shows the diffraction profile for TBPOSS, TCHPOSS, TOPOSS, and DOBPOSS bulk samples, which were analyzed considering triclinic structure using freely available software Expo-2014. 52 The crystal structure solution

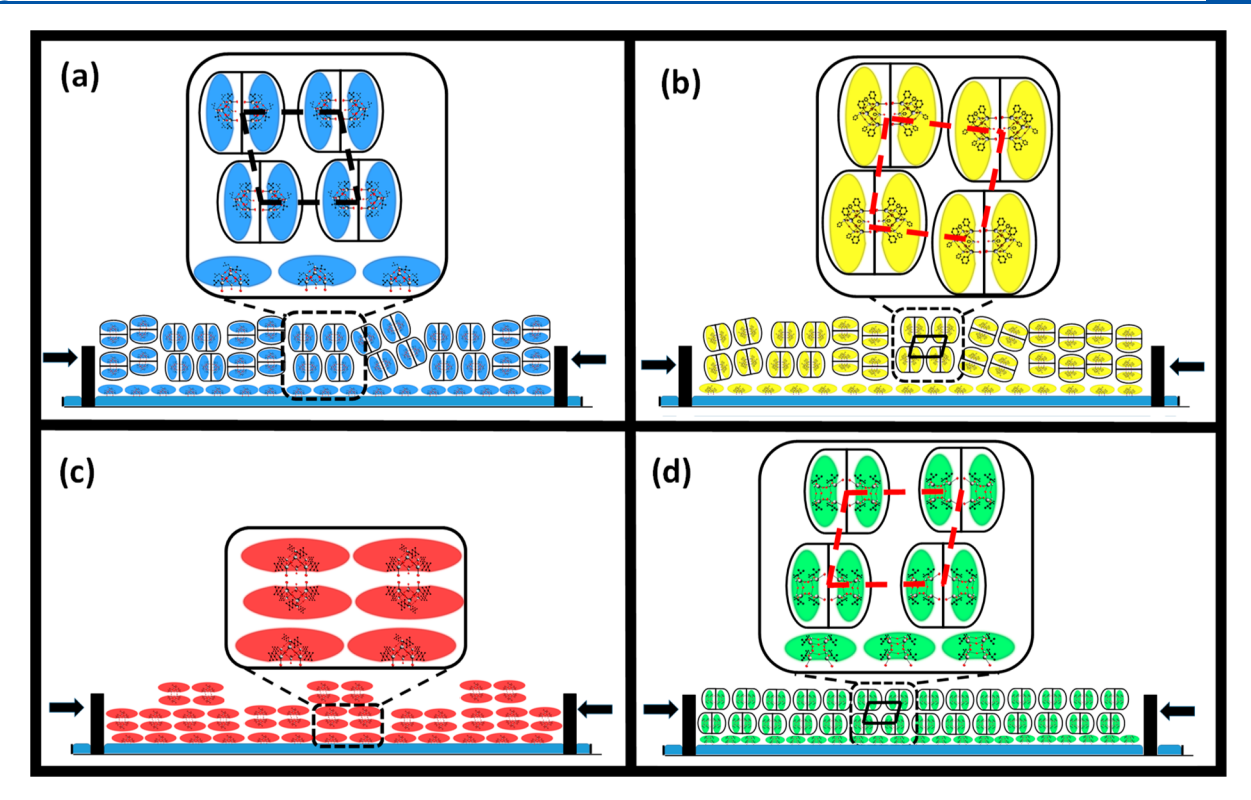


Figure 5. Representation showing the assembly of POSS monomers and dimers forming (a) triclinic lattice structure with a  $P\overline{1}$  symmetry and preferred tilt of crystal planes composed of TBPOSS dimers, postcollapse during the  $2^{nd}$  cycle of compression at surface pressure  $P_{9}$ , (b) crystals of TCHPOSS dimers in a triclinic lattice showing similar preference in alignment with respect to the interface formed postcollapse during the  $2^{nd}$  cycle at surface pressure  $P_{10}$ , (c) compressible multilayers of TOPOSS dimers, exhibiting buckling phenomena at surface pressure  $P_{11}$ , and (d) ordered and oriented single crystal triclinic lattice of DOBPOSS dimers, giving rise to intense diffraction spots at surface pressure  $P_{12}$ .

for TCHPOSS and DOBPOSS (Figure S9(b,d)) is tabulated in Table S3 in the SI. TOPOSS samples in their pristine form exist as a fluid-like material of high viscosity. Neither the pristine sample nor the evaporation dried sample (on a Silicon wafer) exhibited any specific crystallinity, as evident in Figure S9(c). The unit cell volume of TCHPOSS and DOBPOSS are about 2256 ų and 6500 ų, respectively. The cell volume in the bulk powdered form turns out to be smaller than the volume of unit cell formed at the air—water interface. One of the main reasons for this expanded unit cell at the air—water interface is hydrogen bonding.

The structural transitions exhibited by the heptameric POSS framework variants, characterized by in situ GIXS measurements and BAM imaging, reveal crystallization in a triclinic lattice, which is metastable and dynamic in nature. The TCHPOSS layers were observed to transform from a single molecule monolayer to dimeric molecules forming long-ranged 2D ordered layers, to eventually a polycrystalline structure with a definite symmetry formed by dimeric motifs, under the influence of repeated lateral compression-decompression cycles at the air-water interface in a Langmuir trough. The monolayer formation is influenced by the amphiphilic nature of the adjacent monomers. The in-plane and out-of-plane stacking of the bilayers (assembled on top of the monolayer) at different stages of compression can be attributed to the interplay of the hydrophobic vs the hydrophilic interactions. It is observed that post dimerization, the stacking becomes different due to the hydrophobic repulsion among the neighboring dimers. The hydrophilic -OH bonds engage in the dimer formation and are no longer dominant. Finally, we observe the metastable crystallization process of the

TCHPOSS layers at the air-water interface, wherein the dimers (which act as the motif) are now aligned to form the lattice of a triclinic structure with P1 symmetry. The absence of triclinic crystalline states within the TOPOSS layers is attributed to its pristine form of a highly viscous liquid, although it has a similar structure to other heptameric POSS variants. No significant crystalline state is observed in the GIXS, BAM, and XRD measurements on TOPOSS. Alternatively, the octameric POSS framework substituted with eight isobutyl and disilanol bonds exhibits a direct transition into a stable single-crystalline phase. The influence of the POSS core on the ordering and crystallization of differently substituted POSS variants at the air-water interface can be understood in terms of the monomeric size and the symmetry of the POSS monomer. The trisilanol and the disilanol POSS cores differ in their cage structure as they are open-cage T7 and T8 frameworks, respectively. The change in the number of Siatoms changes the monomeric size, symmetry, and the chemical surrounding of the Si-atoms as observed by the <sup>29</sup>Si NMR spectra of the different POSS structures. 53,54 This change in symmetry affects the overall organizational behavior in the POSS systems. The observed dynamic nature of crystallization at the air-water interface corroborates the hydrogen-bonded interaction between the POSS monomers. The complete evolution of the different structural phases of the different POSS variants floating at the air-water interface is followed in situ and quantified using GIXS measurements employing a liquid surface diffractometer.

#### CONCLUSIONS

A variety of structural phases and phase transitions are exhibited by amphiphilic POSS layers at the air-water interface, as evidenced by the nature of the surface pressure versus area per molecule isotherm in successive compression decompression cycles. The nature of phase transitions and subsequent crystallization was observed to be dynamic, mediated by interactions dominated by the ordering specific to a particular phase. These structural phases are followed in situ using GIXS measurements on a Langmuir trough placed atop a liquid surface diffractometer under synchrotron X-ray radiations and complemented by BAM measurements. We observe unique diffraction patterns corresponding to the underlying packing scheme of the heptameric TCHPOSS monomers and dimers ranging from a weakly correlated monolayer to a final polycrystalline powdered form in a triclinic state (with P1 symmetry), mediated by a correlatedbilayer structure. Preferential tilting of the TCHPOSS dimers (angle subtended by the bond-axis with respect to the water surface) are attributes of dominant hydrophobic nearestneighbor interactions of the dimers. The tilting angle changes to a smaller value as a greater number of bilayers are stacked above the existing layers under continued lateral compression. Heptameric TOPOSS layers do not exhibit any distinguishable crystalline structure formation but exhibit high compressibility and buckling in the floating layers. The change in the POSS core framework drastically changes the nature of crystallization resulting in prominent diffraction spots, characteristic of a single crystalline state, as is observed for the octameric DOBPOSS monomers, which exhibit transitions from monolayer to single-crystal like structure. Measurements and quantitative analysis of in situ GIXS profiles reveal important aspects that are imperative to understanding the self-assembly and packing behavior of molecules with tunable amphiphilicity. This study thus provides critical insights into the dynamic nature of the crystallization of amphiphilic molecules at the air-water interface by correlating the differences in the molecules' substitutions to the final crystal structure attained under lateral compression. Such information is crucial for the applicability of POSS molecules in coating and copolymerization processes and other technological applications.

# ASSOCIATED CONTENT

#### Supporting Information

The Supporting Information is available free of charge at https://pubs.acs.org/doi/10.1021/acs.langmuir.1c00420.

Grazing Incidence X-ray Scattering (GIXS) profiles and BAM images of intermediate stages of TCHPOSS structural transformation; GIXS diffractograms obtained postdecompression of floating layers and powder X-ray diffractograms for POSS variants; schematic rendering of the preferred tilt angles of TBPOSS, TCHPOSS crystals, and bilayer configuration of TCHPOSS layer; tabulated list of observed, calculated  $d_{\rm hkl}$  values and corresponding Miller indices for crystals formed at the air—water interface and powdered bulk samples of TCHPOSS and DOBPOSS (PDF)

# AUTHOR INFORMATION

#### **Corresponding Author**

Rupak Banerjee – Department of Physics, Indian Institute of Technology Gandhinagar, Gandhinagar 382355, Gujarat, India; orcid.org/0000-0002-1189-1502; Email: rupakb@iitgn.ac.in

# Authors

Utsav – Department of Physics, Indian Institute of Technology Gandhinagar, Gandhinagar 382355, Gujarat, India

Wei Bu — NSF's ChemMatCARS, University of Chicago, Chicago, Illinois 60637, United States; orcid.org/0000-0002-9996-3733

Binhua Lin — NSF's ChemMatCARS, University of Chicago, Chicago, Illinois 60637, United States; orcid.org/0000-0001-5932-4905

Complete contact information is available at: https://pubs.acs.org/10.1021/acs.langmuir.1c00420

#### **Author Contributions**

U. and R.B. designed and performed the experiments and did the data analysis. B.L. and W.B. supported the experiments and data analysis. The manuscript was written through the contributions of all authors. All authors have approved the final version of the manuscript.

#### Notes

The authors declare no competing financial interest.

## ACKNOWLEDGMENTS

U. and R.B. acknowledge Jawaharlal Nehru Center for Advanced Scientific Research (JNCASR) for full financial support under the Department of Science and Technology India (DST)-Synchrotron-neutron project to carry out experiments at the Advanced Photon Source (APS), Argonne National Lab, U.S.A. They also acknowledge the Central Instrumentation Facility at IIT Gandhinagar for powder XRD measurements. All authors gratefully acknowledge fruitful discussion with Prof. Milan Sanyal (Emeritus Professor, Saha Institute of Nuclear Physics, Kolkata, India) regarding the planning and implementation of this experiment. NSF's ChemMatCARS Sector 15 is supported by the Divisions of Chemistry (CHE) and Materials Research (DMR), National Science Foundation, under grant number NSF/CHE-1834750. Use of the Advanced Photon Source, an Office of Science User Facility operated for the U.S. Department of Energy (DOE) Office of Science by Argonne National Laboratory, was supported by the U.S. DOE under Contract No. DE-AC02-06CH11357.

#### ABBREVIATIONS USED

TBPOSS, Trisilanolisobutyl Polyhedral Silsesquioxane; TCHPOSS, Trisilanolcyclohexyl Polyhedral Silsesquioxane; TOPOSS, Trisilanolisooctyl Polyhedral Silsesquioxane; DOBPOSS, Dislanol Octamericisobutyl Polyhedral Silsesquioxane; GIXS, Grazing Incidence X-ray Scattering; BAM, Brewster's Angle Microscopy

# REFERENCES

- (1) Petty, M. C. Langmuir-Blodgett Films: An Introduction; Cambridge University Press: Cambridge, U.K., 1996.
- (2) Ulman, A. An Introduction to Ultrathin Organic Films: From Langmuir-Blodgett to Self-Assembly; Academic Press: New York, 2013.
  (3) Feher, F. J.; Soulivong, D.; Lewis, G. T. Facile framework cleavage reactions of a completely condensed silsesquioxane frame-
- (4) Feher, F. J.; Budzichowski, T. A.; Blanski, R. L.; Weller, K. J.; Ziller, J. W. Facile syntheses of new incompletely condensed

work. J. Am. Chem. Soc. 1997, 119 (46), 11323-11324.

- polyhedral oligosilsesquioxanes:[(c-C5H9) 7Si7O9 (OH) 3],[(c-C7H13) 7Si7O9 (OH) 3], and [(c-C7H13) 6Si6O7 (OH) 4]. *Organometallics* **1991**, *10* (7), 2526–2528.
- (5) Cordes, D. B.; Lickiss, P. D.; Rataboul, F. Recent developments in the chemistry of cubic polyhedral oligosilsesquioxanes. *Chem. Rev.* **2010**, *110* (4), 2081–2173.
- (6) Barry, A. J.; Daudt, W. H.; Domicone, J. J.; Gilkey, J. W. Crystalline organosilsesquioxanes. J. Am. Chem. Soc. 1955, 77 (16), 4248–4252.
- (7) Dutkiewicz, M.; Karasiewicz, J.; Rojewska, M.; Skrzypiec, M.; Dopierała, K.; Prochaska, K.; Maciejewski, H. Synthesis of an Open-Cage Structure POSS Containing Various Functional Groups and Their Effect on the Formation and Properties of Langmuir Monolayers. Chem. Eur. J. 2016, 22 (37), 13275–13286.
- (8) Imoto, H.; Katoh, R.; Honda, T.; Yusa, S. I.; Naka, K. Self-association behavior of amphiphilic molecules based on incompletely condensed cage silsesquioxanes and poly(ethylene glycol)s. *Polym. J.* **2018**, *50* (4), 337–345.
- (9) Rojewska, M.; Skrzypiec, M.; Prochaska, K. The wetting properties of Langmuir–Blodgett and Langmuir–Schaefer films formed by DPPC and POSS compounds. *Chem. Phys. Lipids* **2019**, 221, 158–166.
- (10) Wang, L.; Du, W.; Wu, Y.; Xu, R.; Yu, D. Synthesis and characterizations of a latent polyhedral oligomeric silsequioxane-containing catalyst and its application in polybenzoxazine resin. *J. Appl. Polym. Sci.* 2012, 126 (1), 150–155.
- (11) Sarkar, B.; Ayandele, E.; Venugopal, V.; Alexandridis, P. Polyhedral oligosilsesquioxane (POSS) nanoparticle localization in ordered structures formed by solvated block copolymers. *Macromol. Chem. Phys.* **2013**, 214 (23), 2716–2724.
- (12) Zhang, D.; Shi, Y.; Liu, Y.; Huang, G. Influences of polyhedral oligomeric silsesquioxanes (POSSs) containing different functional groups on crystallization and melting behaviors of POSS/polydimethylsiloxane rubber composites. *RSC Adv.* **2014**, *4* (78), 41364–41370.
- (13) Zhang, W.; Müller, A. H. Architecture, self-assembly and properties of well-defined hybrid polymers based on polyhedral oligomeric silsesquioxane (POSS). *Prog. Polym. Sci.* **2013**, 38 (8), 1121–1162.
- (14) Teng, C. P.; Mya, K. Y.; Win, K. Y.; Yeo, C. C.; Low, M.; He, C.; Han, M. Y. Star-shaped polyhedral oligomeric silsesquioxane-polycaprolactone-polyurethane as biomaterials for tissue engineering application. NPG Asia Mater. 2014, 6 (11), e142–e142.
- (15) Gon, M.; Sato, K.; Tanaka, K.; Chujo, Y. Controllable intramolecular interaction of 3D arranged  $\pi$ -conjugated luminophores based on a POSS scaffold, leading to highly thermally-stable and emissive materials. *RSC Adv.* **2016**, *6* (82), 78652–78660.
- (16) Zhou, K.; Bisoyi, H. K.; Jin, J. Q.; Yuan, C. L.; Liu, Z.; Shen, D.; Lu, Y. Q.; Zheng, Z. G.; Zhang, W.; Li, Q. Light-Driven Reversible Transformation between Self-Organized Simple Cubic Lattice and Helical Superstructure Enabled by a Molecular Switch Functionalized Nanocage. *Adv. Mater.* **2018**, *30* (26), 1800237.
- (17) Hoflund, G. B.; Gonzalez, R. I.; Phillips, S. H. In situ oxygen atom erosion study of a polyhedral oligomeric silsesquioxane-polyurethane copolymer. *J. Adhes. Sci. Technol.* **2001**, *15* (10), 1199–1211.
- (18) Huang, M.; Hsu, C.-H.; Wang, J.; Mei, S.; Dong, X.; Li, Y.; Li, M.; Liu, H.; Zhang, W.; Aida, T.; Zhang, W.-B.; Yue, K.; Cheng, S. Z. D. Selective assemblies of giant tetrahedra via precisely controlled positional interactions. *Science* **2015**, *348* (6233), 424–428.
- (19) Hartmann-Thompson, C. (Ed.), Applications of polyhedral oligomeric silsesquioxanes; Springer Science & Business Media: New York, 2011; Vol. 3.
- (20) Kalia, S.; Pielichowski, K., Eds.; Polymer/POSS Nanocomposites and Hybrid Materials: Preparation, Properties, Applications; Springer: New York. 2018.
- (21) Deng, J.; Polidan, J. T.; Hottle, J. R.; Farmer-Creely, C. E.; Viers, B. D.; Esker, A. R. Polyhedral oligomeric silsesquioxanes: a new

- class of amphiphiles at the air/water interface. J. Am. Chem. Soc. 2002, 124 (51), 15194–15195.
- (22) Liu, H.; Kondo, S. I.; Tanaka, R.; Oku, H.; Unno, M. A spectroscopic investigation of incompletely condensed polyhedral oligomeric silsesquioxanes (POSS-mono-ol, POSS-diol and POSS-triol): Hydrogen-bonded interaction and host—guest complex. *J. Organomet. Chem.* **2008**, 693 (7), 1301–1308.
- (23) Baney, R. H.; Itoh, M.; Sakakibara, A.; Suzuki, T. Silsesquioxanes. *Chem. Rev.* **1995**, *95* (5), 1409–1430.
- (24) Hu, M. B.; Hou, Z. Y.; Hao, W. Q.; Xiao, Y.; Yu, W.; Ma, C.; Ren, L. J.; Zheng, P.; Wang, W. POM-organic-POSS cocluster: creating a dumbbell-shaped hybrid molecule for programming hierarchical supramolecular nanostructures. *Langmuir* **2013**, 29 (19), 5714–5722.
- (25) Purkayastha, A.; Baruah, J. B. Synthetic methodologies in siloxanes. *Appl. Organomet. Chem.* **2004**, *18* (4), 166–175.
- (26) Morimoto, S.; Imoto, H.; Kanaori, K.; Naka, K. Effect of monosubstituents in heptaisobutyl-substituted polyhedral octasilsesquioxanes on orientationally disordered phase transition. *Bull. Chem. Soc. Jpn.* **2018**, *91* (9), 1390–1396.
- (27) Feher, F. J.; Soulivong, D.; Lewis, G. T. Facile framework cleavage reactions of a completely condensed silsesquioxane framework. J. Am. Chem. Soc. 1997, 119 (46), 11323–11324.
- (28) Feher, F. J.; Terroba, R.; Ziller, J. W. A new route to incompletely-condensed silsesquioxanes: base-mediated cleavage of polyhedral oligosilsesquioxanes. *Chem. Commun.* 1999, 22, 2309—2310
- (29) Wu, B.; Zhang, Y.; Yang, D.; Yang, Y.; Yu, Q.; Che, L.; Liu, J. Self-healing anti-atomic-oxygen phosphorus-containing polyimide film via molecular level incorporation of nanocage trisilanolphenyl POSS: preparation and characterization. *Polymers* **2019**, *11* (6), 1013.
- (30) Wang, P.; Tang, Y.; Yu, Z.; Gu, J.; Kong, J. Advanced aromatic polymers with excellent antiatomic oxygen performance derived from molecular precursor strategy and copolymerization of polyhedral oligomeric silsesquioxane. ACS Appl. Mater. Interfaces 2015, 7 (36), 20144–20155.
- (31) Banerjee, R.; Sanyal, M. K.; Bera, M. K.; Gibaud, A.; Lin, B.; Meron, M. Reversible monolayer-to-crystalline phase transition in amphiphilic silsesquioxane at the air-water interface. *Sci. Rep.* **2015**, *5* (1), 1–8.
- (32) Clark, J. H. Reversible crystallization in tendons and its functional significance. *Proc. Natl. Acad. Sci. U. S. A.* **1928**, *14* (7), 526.
- (33) Edman, K.; Nollert, P.; Royant, A.; Belrhali, H.; Pebay-Peyroula, E.; Hajdu, J.; Neutze, R.; Landau, E. M. High-resolution X-ray structure of an early intermediate in the bacteriorhodopsin photocycle. *Nature* **1999**, *401* (6755), 822–826.
- (34) Terada, S.; Xin, Y.; Saitow, K. I. Cost-Effective Synthesis of Silicon Quantum Dots. *Chem. Mater.* 2020, 32 (19), 8382–8392.
- (35) Hessel, C. M.; Henderson, E. J.; Veinot, J. G. Hydrogen silsesquioxane: a molecular precursor for nanocrystalline Si– SiO2 composites and freestanding hydride-surface-terminated silicon nanoparticles. *Chem. Mater.* **2006**, *18* (26), 6139–6146.
- (36) Yue, K.; Liu, C.; Guo, K.; Yu, X.; Huang, M.; Li, Y.; Wesdemiotis, C.; Cheng, Z. D. S.; Zhang, W. B. Sequential "click" approach to polyhedral oligomeric silsesquioxane-based shape amphiphiles. *Macromolecules* **2012**, 45 (20), 8126–8134.
- (37) Deng, J.; Farmer-Creely, C. E.; Viers, B. D.; Esker, A. R. Unique rodlike surface morphologies in trisilanolcyclohexyl polyhedral oligomeric silsesquioxane films. *Langmuir* **2004**, *20* (7), 2527–2530.
- (38) Lichtenhan, J. D.; Vu, N. Q.; Carter, J. A.; Gilman, J. W.; Feher, F. J. Silsesquioxane-siloxane copolymers from polyhedral silsesquioxanes. *Macromolecules* **1993**, *26* (8), 2141–2142.
- (39) Boccaleri, E., Carniato, F. Synthesis routes of poss. In *Polymer/POSS Nanocomposites and Hybrid Materials*; Springer: Cham, 2018; pp 1–26.
- (40) Waddon, A. J.; Coughlin, E. B. Crystal structure of polyhedral oligomeric silsequioxane (POSS) nano-materials: a study by X-ray

- diffraction and electron microscopy. Chem. Mater. 2003, 15 (24), 4555-4561.
- (41) Heeley, E. L.; Hughes, D. J.; El Aziz, Y.; Taylor, P. G.; Bassindale, A. R. Linear long alkyl chain substituted POSS cages: the effect of alkyl chain length on the self-assembled packing morphology. *Macromolecules* **2013**, *46* (12), 4944–4954.
- (42) Kaganer, V. M.; Möhwald, H.; Dutta, P. Structure and phase transitions in Langmuir monolayers. *Rev. Mod. Phys.* **1999**, *71* (3), 779.
- (43) Dutta, P. Phase transitions in lipid monolayers on water: new light on an old problem. In *Phase Transitions in Surface Films* 2; Springer: Boston, MA, 1991; pp 183–200.
- (44) Feher, F. J.; Newman, D. A.; Walzer, J. F. Silsesquioxanes as models for silica surfaces. J. Am. Chem. Soc. 1989, 111 (5), 1741–1748.
- (45) Heeley, E. L.; Hughes, D. J.; El Aziz, Y.; Williamson, I.; Taylor, P. G.; Bassindale, A. R. Properties and self-assembled packing morphology of long alkyl-chained substituted polyhedral oligomeric silsesquioxanes (POSS) cages. *Phys. Chem. Chem. Phys.* **2013**, *15* (15), 5518–5529.
- (46) El Aziz, Y.; Bassindale, A. R.; Taylor, P. G.; Stephenson, R. A.; Hursthouse, M. B.; Harrington, R. W.; Clegg, W. X-ray crystal structures, packing behavior, and thermal stability studies of a homologous series of n-alkyl-substituted polyhedral oligomeric silsesquioxanes. *Macromolecules* **2013**, 46 (3), 988–1001.
- (47) Lombardo, D.; Kiselev, M. A.; Magazù, S.; Calandra, P. Amphiphiles self-assembly: basic concepts and future perspectives of supramolecular approaches. *Adv. Condens. Matter Phys.* **2015**, 2015, 1–22.
- (48) Degiorgio, V. Physics of Amphiphiles, Micelles and Microemulsions. *Europhys. News* **1985**, *16* (6), 9–12.
- (49) Bera, M. K.; Sanyal, M. K.; Pal, S.; Daillant, J.; Datta, A.; Kulkarni, G. U.; Luzet, D.; Konovalov, O. Reversible buckling in monolayer of gold nanoparticles on water surface. *EPL (Europhysics Letters)* **2007**, 78 (5), 56003.
- (50) Banerjee, R.; Hazra, S.; Banerjee, S.; Sanyal, M. K. Nanopattern formation in self-assembled monolayers of thiol-capped Au nanocrystals. *Phys. Rev. E* **2009**, *80* (5), No. 056204.
- (51) Banerjee, R.; Sanyal, M. K.; Bera, M. K.; Singh, A.; Novak, J.; Konovalov, O. Structural reordering in monolayers of gold nanoparticles during transfer from water surface to solid substrate. *Phys. Rev. E* **2011**, 83 (5), No. 051605.
- (52) Altomare, A.; Cuocci, C.; Giacovazzo, C.; Moliterni, A.; Rizzi, R.; Corriero, N.; Falcicchio, A. EXPO2013: a kit of tools for phasing crystal structures from powder data. *J. Appl. Crystallogr.* **2013**, *46* (4), 1231–1235.
- (53) Wu, K.; Song, L.; Hu, Y.; Lu, H.; Kandola, B. K.; Kandare, E. Synthesis and characterization of a functional polyhedral oligomeric silsesquioxane and its flame retardancy in epoxy resin. *Prog. Org. Coat.* **2009**, *65* (4), 490–497.
- (54) Mantz, R. A.; Jones, P. F.; Chaffee, K. P.; Lichtenhan, J. D.; Gilman, J. W.; Ismail, I. M. K.; Burmeister, M. J. Thermolysis of polyhedral oligomeric silsesquioxane (POSS) macromers and POSS–siloxane copolymers. *Chem. Mater.* **1996**, *8* (6), 1250–1259.